

Diffusion Imaging

Konstantinos Arfanakis, PhD

Assistant Professor
Department of Biomedical Engineering
Illinois Institute of Technology
10 West 32nd Street
E1-116
Chicago, IL 60616

1 Introduction

Diffusion tensor imaging (DTI), as implemented in MRI (1,2), is a noninvasive imaging technique that can be used in order to probe, *in vivo*, the intrinsic diffusion properties of deep tissues. DTI has been applied in several studies to infer the microstructural characteristics of the brain (3-6), the heart (7-10), muscle tissue (11-13), bone marrow (14), intervertebral discs (15), and the spinal cord (16-18). Brain function (19,20) and development of human cerebral white matter in newborns (21-23) are also areas of research with growing interest in DTI. In addition, DTI may assist diagnosis of disease conditions such as cerebral ischemia (24-25), acute stroke (26,27), multiple sclerosis (28-30), schizophrenia (31) and traumatic brain injury (32,33).

Unlike conventional diffusion imaging (DI) (34), where diffusion-weighted (DW) images are used to calculate an apparent scalar diffusion constant (ADC), DTI characterizes diffusive transport of water by an effective diffusion tensor **D**. This symmetric 3x3 tensor is of great importance since it contains useful structural information about the tissue. The eigenvalues of **D** are the three principal diffusivities and the eigenvectors define the local

fiber tract direction field (1). Moreover, one can derive from \mathbf{D} rotationally invariant scalar quantities that describe the intrinsic diffusion properties of the tissue. The most commonly used are the trace of the tensor (1, 3, 35), which measures mean diffusivity, Fractional Anisotropy (FA), Relative Anisotropy (RA) (3, 35, 36), Volume Ratio (VRat) and Lattice Index (LI) (36, 37), which all characterize the anisotropy of the fiber structure.

Precision in the estimation of the elements of the diffusion tensor, and consequently of the scalar quantities derived from it, is crucial for many DTI studies. Examples of DTI applications that are particularly sensitive to any type of errors are: diagnosis of acute stroke using the trace of \mathbf{D} (26,27), or white matter fiber tracking based on the eigenvectors and eigenvalues of \mathbf{D} (38-43). The noise content of the MR signal affects the accuracy of DTI results. Noise existing in the acquired DW images propagates to the elements of the diffusion tensor \mathbf{D} and to the scalar quantities that describe the diffusion properties of the tissue. In order to overcome this problem various acquisition schemes have been proposed with different combinations of DW gradient orientations, diffusion weightings and number of repetitions of each acquisition (44,45). Post processing noise reduction techniques (46), as well as high field magnets, have also been used to improve SNR. Head motion has also been a source of significant artifacts in DTI. Various pulse sequences have been developed in an attempt to eliminate motion related artifacts from DTI studies (47). An additional problem, originating from the high gradient amplitudes used in DTI, has been the eddy current artifacts. To minimize eddy currents special pulse sequences (48-51) and post processing algorithms (52,53) have been implemented.

2 Data acquisition for DTI

2.1 DTI pulse sequence

The pulse sequence that is commonly used to acquire DTI data is a two-dimensional spin-echo sequence with an EPI acquisition window and a pair of DW gradients (Fig.1). The DW gradients are symmetrically positioned around the 180° RF pulse. Following the 90° pulse there is negligible loss of phase coherence until the first DW gradient is applied.

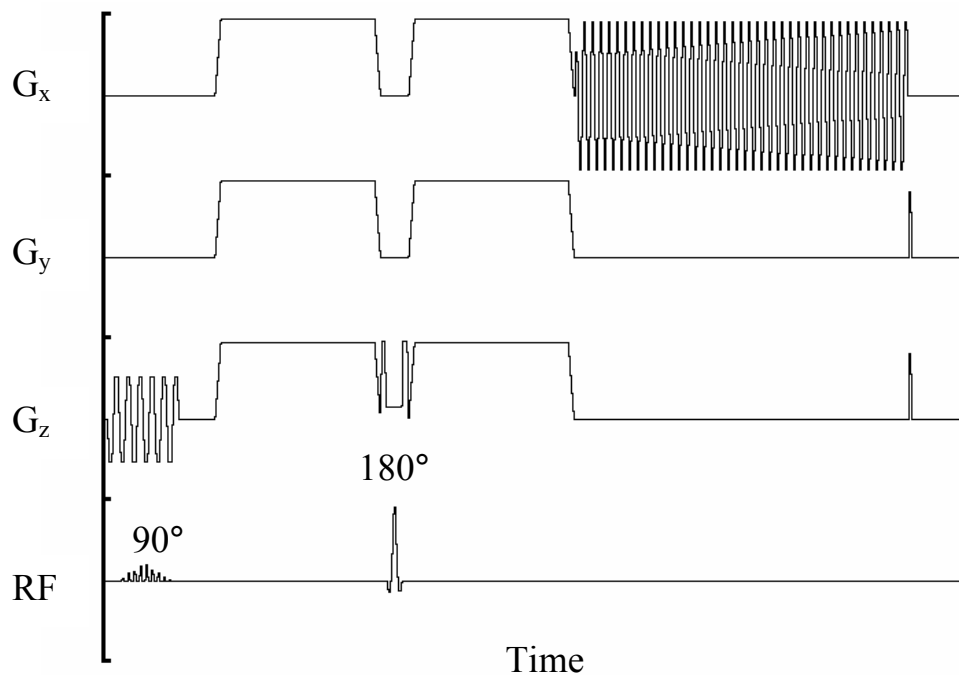


Figure 1. Basic pulse sequence for DTI acquisition. The DW gradients are shown to be activated in all three directions and with maximum amplitude. In reality, during execution of the sequence the amplitudes of the DW gradients change relative to each other in order to sensitize diffusion in different orientations in three-dimensional space. The blips in the phase encoding gradient during readout are not visible due to their low amplitude.

This gradient produces a phase shift, which depends on the position of the protons in the direction of the applied DW gradient. After the first DW gradient is turned off there is again negligible loss of phase coherence. However, the protons change position while they diffuse. The 180° RF pulse inverts the phase shifts, and the second DW gradient produces phase shifts equal to those produced by the first DW gradient. If the protons would not diffuse then the second DW gradient, due to the presence of the 180° RF pulse, would undo the effect of the first DW gradient. Diffusion causes the refocusing to be incomplete. In voxels that exhibit high diffusion along the direction of the applied DW gradient, the intensity in the corresponding DW image is reduced compared to that of voxels with lower diffusivity along the same direction. Only the changes in position occurring between the two DW gradients are important and are equally weighted regardless of when they occur within this interval (54). Additionally, the time between the two DW gradients should be set according to the scale of diffusion under study. In other words, this interval cannot be infinitely small since the protons will not have enough time to reach the anatomical limits of diffusion and they will appear as they equally diffuse towards any direction (isotropic diffusion). On the other hand the time between the two DW gradients cannot be very large since, besides loss of signal due to T2 decay, the protons will significantly change position and the loss of signal due to incomplete refocusing will be massive.

2.2 Acquisition schemes

In the sequence described above, the diffusion weighting is determined by the amplitude

of the total DW gradient \mathbf{G} , where $\mathbf{G} = (G_x, G_y, G_z)$, the duration of the DW gradient lobes and their temporal spacing. To achieve the lowest possible TE, the amplitude of the DW gradients is maximized and their duration is minimized, maintaining at the same time the necessary diffusion weighting. By changing the amplitudes of the DW gradients in all three directions (readout, phase encoding, slice select) simultaneously, while keeping the amplitude of the total DW gradient \mathbf{G} the same, it is possible to sensitize diffusion in any direction in three-dimensional space. Four different DTI acquisition schemes are shown below. These schemes employ different combinations of DW gradient orientations and the same diffusion weighting. Schemes a, b, c, d include 6, 11, 23, 46 DW gradient orientations respectively (Fig. 2).

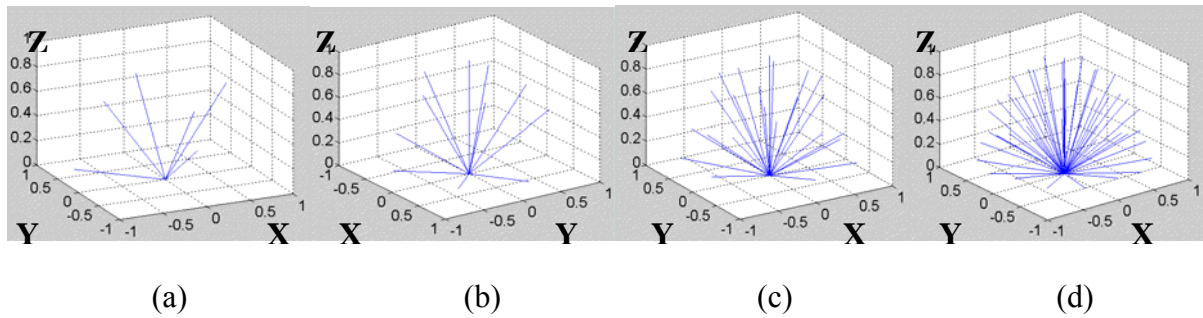


Figure 2. DW gradient orientations for acquisition schemes a, b, c, d. All vectors have unit length. Only half of the three-dimensional space is shown.

3 Post processing for DTI

3.1 Estimation of the effective diffusion tensor \mathbf{D}

The primary goal of a DTI experiment is to estimate the elements of the effective diffusion tensor \mathbf{D} in each voxel. The diffusion tensor is a symmetric 3x3 matrix of the form:

$$\mathbf{D} = \begin{bmatrix} D_{xx} & D_{xy} & D_{xz} \\ D_{yx} & D_{yy} & D_{yz} \\ D_{zx} & D_{zy} & D_{zz} \end{bmatrix} \quad [1]$$

Thus, calculating the six elements D_{xx} , D_{yy} , D_{zz} , D_{xy} , D_{xz} , D_{yz} , fully determines \mathbf{D} .

For the DTI experiment the following equation applies for each voxel:

$$\ln\left(\frac{S}{S_0}\right) = -\sum_{i=1}^3 \sum_{j=1}^3 b_{ij} D_{ij}, \quad [2]$$

where S is the DW signal intensity, S_0 is the spin-echo signal when no diffusion gradient is applied, b_{ij} are elements of the \mathbf{b} matrix (2) and D_{ij} are elements of the diffusion tensor \mathbf{D} . The \mathbf{b} matrix is also a 3x3 matrix. For the gradient pulses that are commonly used in DTI pulse sequences simple analytic expressions can be derived for b_{ij} . For the trapezoidal DW gradients that are used in the pulse sequence described earlier, b_{ij} is given by:

$$b_{ij} = \gamma^2 G_i G_j \left[\delta^2 \left(\Delta - \frac{\delta}{3} \right) + \frac{\varepsilon^3}{30} - \frac{\delta \varepsilon^2}{6} \right], \quad [3]$$

where γ is the gyromagnetic ratio of protons, δ is the time between the start of the initial ramp of a trapezoidal DW gradient and the end of its plateau, Δ is the time between the initial rise of the first and second DW gradients, and ε is the rise time of the ramp.

From Eq. [2], the system can be fully determined with acquisition of at least 6 non-collinear DW orientations and an additional T2 image. This acquisition scheme is sufficient for a robust estimation of the diffusion tensor \mathbf{D} . If more than 6 non-collinear directions are

acquired, the system is overdetermined and can be solved using linear (eg. singular value decomposition) or non-linear (eg. Levenberg-Marquardt) approaches (55).

3.2 Scalar invariants of \mathbf{D}

Eigenvalues and eigenvectors of \mathbf{D}

The corresponding eigenvalues $\lambda_1, \lambda_2, \lambda_3$, and eigenvectors $\mathbf{e}_1, \mathbf{e}_2, \mathbf{e}_3$ of the diffusion tensor \mathbf{D} of a voxel can be derived by:

$$\mathbf{D} \mathbf{e}_i = \lambda_i \mathbf{e}_i \quad , i = 1, 2, 3 . \quad [4]$$

Because \mathbf{D} is symmetric and positive definite (1), its eigenvectors $\mathbf{e}_1, \mathbf{e}_2, \mathbf{e}_3$ are orthogonal. The eigenvectors of \mathbf{D} define the local fiber tract direction field and the corresponding eigenvalues are the effective diffusivities in these directions.

Trace of \mathbf{D}

One rotationally invariant scalar quantity that can be derived from the diffusion tensor \mathbf{D} , for each voxel, is the Trace (1, 3, 35). The Trace is equal to:

$$\text{Trace} = \lambda_1 + \lambda_2 + \lambda_3 = 3 \langle \mathbf{D} \rangle , \quad [5]$$

where $\langle \mathbf{D} \rangle$ is the mean diffusivity.

Fractional anisotropy (FA)

Another rotationally invariant scalar quantity that can be derived from the diffusion tensor \mathbf{D} is the FA (3, 35, 36):

$$FA = \sqrt{\frac{3}{2} \frac{\sqrt{\frac{1}{3}((\lambda_1 - \lambda_2)^2 + (\lambda_2 - \lambda_3)^2 + (\lambda_3 - \lambda_1)^2)}}{\sqrt{\lambda_1^2 + \lambda_2^2 + \lambda_3^2}}} . \quad [6]$$

FA measures diffusion anisotropy of fiber structure. FA owes its name to the fact that it expresses the ratio of the anisotropic part of the diffusion tensor \mathbf{D} over the total magnitude of the tensor. For any material:

$$0 \leq FA \leq 1 . \quad [7]$$

The minimum value of FA can occur only in a perfectly isotropic medium. The maximum value can occur only when $\lambda_1 \gg \lambda_2 = \lambda_3$ (20).

Relative anisotropy (RA)

RA is also a rotationally invariant scalar quantity (3, 35, 36) that measures diffusion anisotropy of fiber structure. It is given by:

$$RA = \frac{\sqrt{((\lambda_1 - \lambda_2)^2 + (\lambda_2 - \lambda_3)^2 + (\lambda_3 - \lambda_1)^2)}}{\lambda_1 + \lambda_2 + \lambda_3} , \quad [8]$$

For an isotropic medium $RA = 0$. RA expresses the ratio of the anisotropic part of the diffusion tensor \mathbf{D} over the isotropic part of \mathbf{D} .

Volume ratio (VRat)

VRat is given by:

$$\text{VRat} = 27 \frac{\lambda_1 \lambda_2 \lambda_3}{(\lambda_1 + \lambda_2 + \lambda_3)^3} . \quad [9]$$

VRat is a rotationally scalar invariant quantity that measures diffusion anisotropy of fiber structure (37). VRat represents the volume of an ellipsoid whose semimajor axes are the three eigenvalues of \mathbf{D} divided by the volume of a sphere whose radius is the mean diffusivity $\langle D \rangle$. For an isotropic medium $\text{VRat} = 1$, and as anisotropy increases VRat approaches 0. This behavior is opposite than that of FA and RA which increase as anisotropy increases. Therefore, since VRat describes similar properties, maps of 1-VRat are usually constructed.

Linearity

High diffusion anisotropy can be achieved while the three eigenvalues define an oblate or a prolate diffusion ellipsoid. FA, RA and VRat cannot differentiate between the different shapes. In contrast, linearity is a rotationally scalar invariant quantity that increases as the diffusion ellipsoid becomes more prolate (56). Linearity is given by:

$$\text{Linearity} = \frac{\lambda_1 - \lambda_2}{\lambda_1 + \lambda_2 + \lambda_3} . \quad [10]$$

For an isotropic medium linearity = 0. As the diffusion ellipsoid becomes more prolate linearity approaches the value 1.

Planar Index

Planar index is a rotationally scalar invariant quantity that increases as the diffusion ellipsoid becomes more oblate (57). The value of the planar index is given by:

$$\text{Planar} = 2 \frac{\lambda_2 - \lambda_3}{\lambda_1 + \lambda_2 + \lambda_3} \quad [11]$$

For any material the value of the planar index ranges between 0 and 1. For a medium with $\lambda_1 = \lambda_2$, and $\lambda_3 = 0$, the planar index = 1. In contrast, if $\lambda_2 = \lambda_3$ the planar index becomes 0.

Lattice Index

For two neighboring voxels with diffusion tensors \mathbf{D} and \mathbf{D}' , the tensor dot product is:

$$\mathbf{D} : \mathbf{D}' = \sum_{k=1}^3 \sum_{s=1}^3 \lambda_k \lambda'_s \left(\mathbf{e}_k^T \mathbf{e}_s \right)^2, \quad [12]$$

where λ_k , λ'_s and \mathbf{e}_k , \mathbf{e}_s are the eigenvalues and eigenvectors of \mathbf{D} and \mathbf{D}' respectively. The tensor dot product between the anisotropic parts of the diffusion tensors can be written as:

$$\mathbf{D} : \mathbf{D}' = \mathbf{D} : \mathbf{D}' - \frac{1}{3} \text{Trace}(\mathbf{D}) \text{Trace}(\mathbf{D}'). \quad [13]$$

For a reference voxel (ref) and an arbitrary neighboring voxel (N) the Lattice Index (LI_N) (36,37) is defined as:

$$\text{LI}_N = \frac{\sqrt{3}}{\sqrt{8}} \frac{\sqrt{\mathbf{D}_{ref} : \mathbf{D}_N}}{\sqrt{\mathbf{D}_{ref} : \mathbf{D}_N}} + \frac{3}{4} \frac{\mathbf{D}_{ref} : \mathbf{D}_N}{\sqrt{\mathbf{D}_{ref} : \mathbf{D}_{ref}} \sqrt{\mathbf{D}_N : \mathbf{D}_N}}. \quad [14]$$

An average LI can be computed for each voxel by calculating LI_N for the reference voxel and each of the eight, in plane, contiguous voxels, and then weighting their contributions

according to their distance from the reference voxel:

$$LI_{\text{ref}} = \frac{\sum_{N=1}^8 a_N LI_N}{\sum_{N=1}^8 a_N}, \quad [15]$$

where LI_{ref} is the average LI for the reference voxel and a_N is a weighting factor which is equal to 1 for voxels that share a side with the reference voxel and $\frac{1}{\sqrt{2}}$ for voxels that share a vertex with the reference voxel.

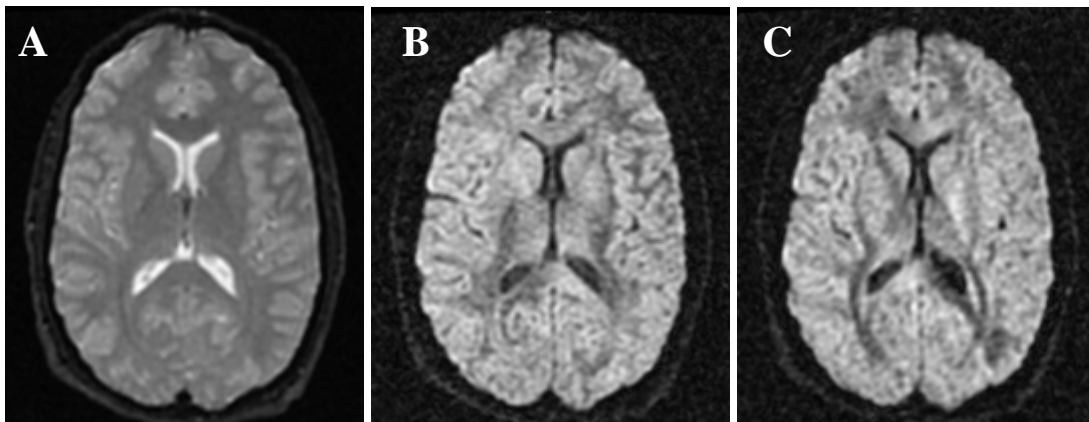
LI is a local intervoxel anisotropy index. It ranges from 0, for isotropic media, to 1, for media with $\lambda_1 \neq 0, \lambda_2 = \lambda_3 = 0$. LI is proven (37) to lessen the effect of noise in the final diffusion anisotropy maps, without introducing the artifacts caused by averaging the signal intensity over the entire ROI. One potential disadvantage of using LI is that if spatial resolution is low then LI might be averaging information from very different types of tissue.

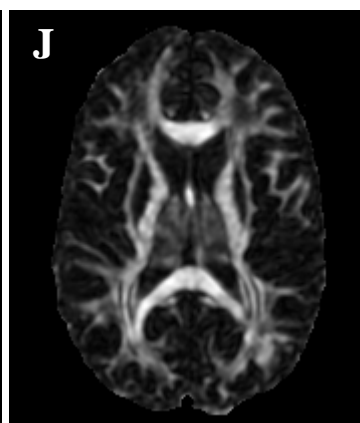
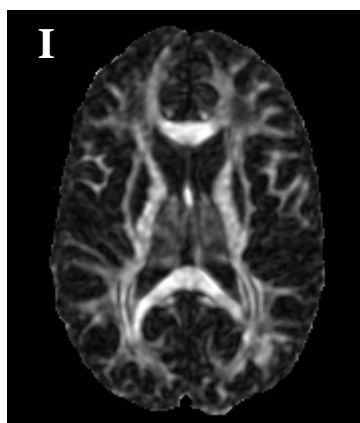
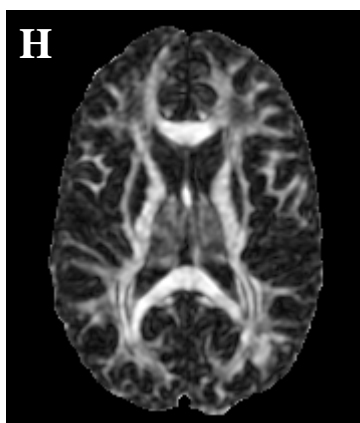
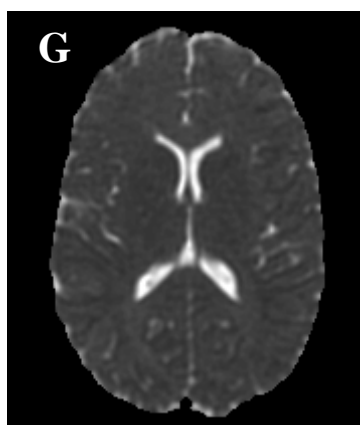
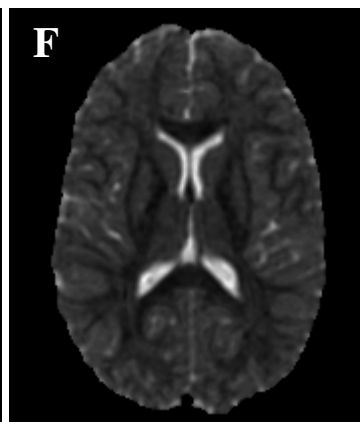
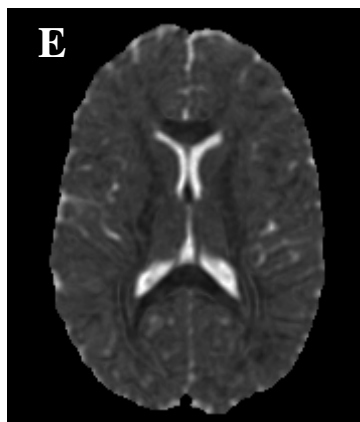
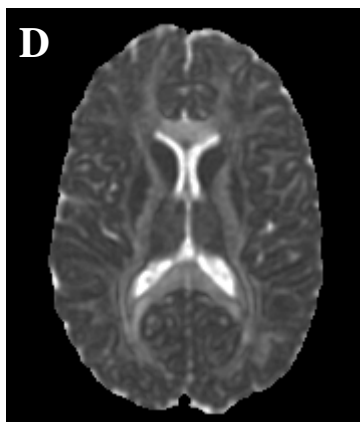
4 Visualization of DTI results

The following images were obtained from DTI scans performed on a clinical 1.5T GE scanner with high-speed gradients (40 mT/m maximum amplitude, 150 mT/m/msec slew rate). The DTI data acquisition and post-processing software were developed in our lab. The imaging parameters were TR = 4500ms, TE = 71.8ms, field of view = 24cm x 24cm, 21 contiguous slices, 3mm slice thickness. The amplitude of the total diffusion gradient was 40 mT/m and for the example shown below was applied in 46 non-collinear directions uniformly distributed in three-dimensional space. The duration of each DW gradient lobe

was 21.3ms and their temporal spacing was 26.9ms. The effective diffusion weighting was $b=1000 \text{ sec/mm}^2$. T2 images with no diffusion weighting ($b=0 \text{ sec/mm}^2$) were also acquired at the beginning of the DTI scan. Echo planar readout was performed with a 128×128 image matrix and all images were reconstructed to a 256×256 matrix after zero filling. Therefore, the resultant voxel dimensions were $0.9375 \times 0.9375 \times 3 \text{ mm}^3$. For the example shown below, all DW images ($b=1000 \text{ sec/mm}^2$) were acquired 2 times and the T2 images were repeated 14 times. The duration of the scan was 7 minutes and 57 seconds.

Figure 3 shows examples of T2, DW, λ_1 , λ_2 , λ_3 , trace, FA, RA, LI, 1-VRat, linearity, planar index maps, for an axial slice of a healthy volunteer.





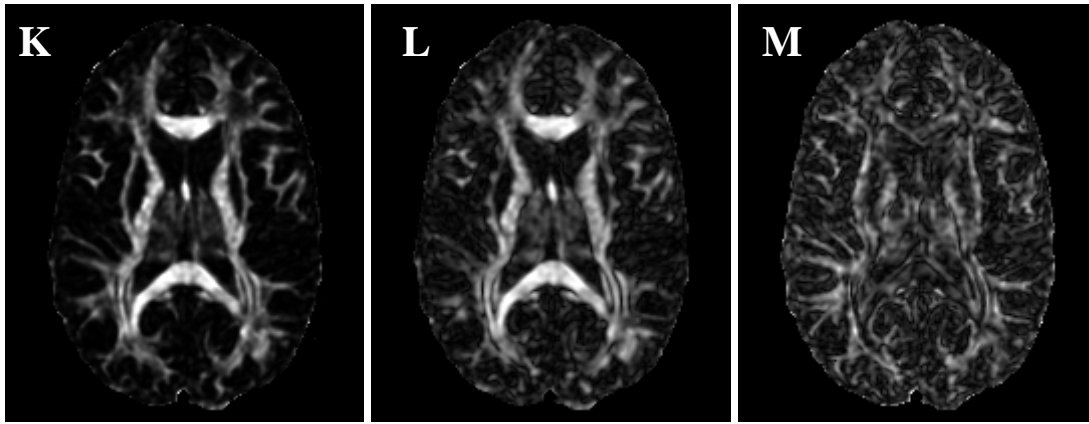


Figure 3. T2W (A), 2 of the 46 DW (B) and (C), λ_1 (D), λ_2 (E), λ_3 (F), trace (G), FA (H), RA (I), LI (J), 1-VRat (K), linearity (L), planar (M) maps for an axial slice of a healthy volunteer.

In regions with tightly packed white matter fibers (e.g. corpus callosum), the eigenvalue maps exhibit high intensities for λ_1 and lower for λ_2 and λ_3 which is characteristic for very anisotropic diffusion of protons. In regions of high diffusion with no preferred direction (e.g. ventricles), the eigenvalue maps exhibit high intensities for λ_1 , λ_2 and λ_3 which are also almost equal to each other. Trace maps demonstrate high intensities for regions with high mean diffusivity (e.g. ventricles). Small differences exist in trace maps between gray and white matter since the mean diffusivity values for these two types of tissue are very similar to each other. FA and RA maps contain similar information with each other. They demonstrate high diffusion anisotropy for white matter structures and low anisotropy for gray matter and CSF. Regions like the corpus callosum, the left and right internal capsule, the left and right external capsule, the optic radiations and other major white matter fiber tracts exhibit the highest values of diffusion anisotropy. LI maps contain similar information with FA and RA maps but significantly less noise. Maps of 1-VRat contain similar information to FA, RA and

LI but with higher contrast. Linearity maps reveal the regions that are characterized by highly prolate diffusion ellipsoids. Planar maps demonstrate the regions characterized by oblate diffusion ellipsoids.

Maps of quantities that measure diffusion anisotropy are essentially maps of white matter. However, they provide no information about the orientation of the white matter fibers. One way to display directional information is by assigning colors to specific directions in three-dimensional space and displaying maps in which each voxel is colored in accordance to the correspondence of colors and primary diffusion directions. In Absolute Value maps (58), the x, y, z directions are assigned red, green and blue colors respectively, and any other direction within the xyz octant is assigned a combination of red, green and blue. This means that each color appears once in each octant of three-dimensional space. Therefore, fibers with rotational or mirror symmetry appear to have the same color. The brightness of each voxel is finally scaled by its LI value. An example of an Absolute Value map is shown in Figure 4a. The correspondence of colors and directions is presented by the colored circle of Figure 4b. For axial slices, the colored circle should be thought of as a dome seen from underneath with the viewer standing at the center of the dome. Then, each color corresponds to a direction that is parallel to the axis that connects the viewer to the point on the surface of the dome with the same color. Therefore, the colored circle serves as a look-up table of primary diffusion directions.

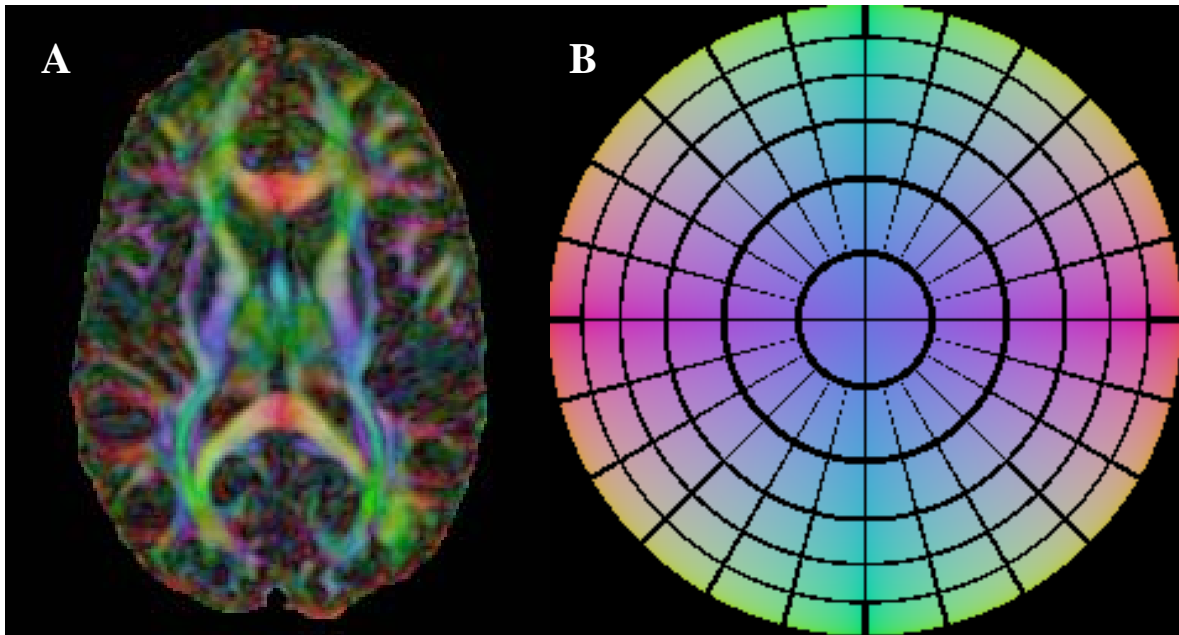


Figure 4. (a) Absolute Value map for an axial slice of a normal volunteer. (b) Color circle for Absolute Value map.

6 Corrections in DTI acquisitions

6.1 Contribution of imaging gradients to diffusion weighting

Diffusion weighting in DW images is achieved by the use of diffusion gradients. However, diffusion and imaging gradients interact with one another, producing additional cross terms in the b factor (59). Therefore, the final b value is slightly higher than the expected value. If no correction is performed this can lead to an incorrect estimate of the diffusion coefficient.

6.2 Eddy current induced artifacts

In DTI experiments, whenever a strong DW gradient is turned on or off, eddy currents are induced in conductive parts of the magnet bore and its surroundings. Residual eddy-current-induced gradient fields during the echo-planar readout, cause geometric distortions in the phase encoding direction of DW images (shearing, scaling, translation). These geometric distortions produce misalignments between the individual DW images of the DTI dataset, which eventually lead to artifacts in the computed maps of the diffusion parameters.

Different pulse sequences (48-51) and post-processing algorithms (52,53) have been implemented to minimize eddy current artifacts. A relatively simpler and effective approach to reduce eddy-current distortions is to register all DW images to the mean DW image for each slice, using a 2D registration algorithm.

References

1. Basser PJ, Mattiello J, Le Bihan D. MR diffusion tensor spectroscopy and imaging. *Biophys J* 1994;66:259-267.
2. Basser PJ, Mattiello J, Le Bihan D. Estimation of the effective self-diffusion tensor from the NMR spin echo. *J Magn Reson B* 1994;103:247-254.
3. Pierpaoli C, Jezzard P, Basser PJ, Barnett A, Di Chiro G. Diffusion tensor MR imaging of the human brain. *Radiology* 1996;201:637-648.
4. Peled S, Gudbjartsson H, Westin CF, Kikinis R, Jolesz FA. Magnetic resonance imaging shows orientation and asymmetry of white matter fiber tracts. *Brain Res* 1998;780:27-33.

5. Virta A, Barnett A, Pierpaoli C. Visualizing and characterizing white matter fiber structure and architecture in the human pyramidal tract using diffusion tensor MRI. *Magn Reson Imaging* 1999;17:1121-1133.
6. Bahn MM. A linear relationship exists among brain diffusion eigenvalues measured by diffusion tensor magnetic resonance imaging. *J Magn Reson* 1999;137:33-38.
7. Holmes AA, Scollan DF, Winslow RL. Direct histological validation of diffusion tensor MRI in formaldehyde-fixed myocardium. *Magn Reson Med* 2000;44:157-161.
8. Garrido L, Wedeen VJ, Kwong KK, Spencer UM, Kantor HL. Anisotropy of water diffusion in the myocardium of the rat. *Circ Res* 1994;74:789-793.
9. Hsu EW, Muzikant AL, Matulevicius SA, Penland RC, Henriquez CS. Magnetic resonance myocardial fiber orientation mapping with direct histological correlation. *Am J Physiol* 1998;274:H1627-H1634.
10. Scollan DF, Holmes AA, Winslow RL, Forder J. Histological validation of myocardial microstructure obtained from diffusion tensor magnetic resonance imaging. *Am J Physiol* 1998;275:H2308-H2318.
11. van Donkelaar CC, Kretzers LJ, Bovendeerd PHM, Lataster LM, Nicolay K, Janssen JD, Drost MR. Diffusion tensor imaging in biomechanical studies of skeletal muscle function. *J Anat* 1999;194:79-88.
12. van Gelderen P, Despres D, van Zijl PCM, Moonen CTW. Evaluation of restricted diffusion in cylinders. Phosphocreatine in rabbit leg muscle. *J Magn Reson* 1994;103:255-260.

13. van Doorn A; Bovendeerd PHM, Nicolay K, Drost MR, Janssen JD. Determination of muscle fiber orientation using diffusion-weighted MRI. *Eur J Morphol* 1996;34:5-10.
14. Baur A, Stabler A, Bruning R, Bartl R, Krodel A, Reiser M, Deimling M. Diffusion-weighted MR imaging of bone marrow: differentiation of benign versus pathologic compression fractures. *Radiology* 1998;207:349-356.
15. Hsu EW, Setton LA. Diffusion tensor microscopy of the intervertebral disc anulus fibrosus. *Magn Reson Med* 1999;41:992-999.
16. Fenyves DA, Narayana PA. In vivo diffusion tensor imaging of rat spinal cord with echo planar imaging. *Magn Reson Med* 1999;42:300-306.
17. Gulani V, Iwamoto GA, Jiang H, Shimony JS, Webb AG, Lauterbur PC. A multiple echo pulse sequence for diffusion tensor imaging and its application in excised rat spinal cords. *Magn Reson Med* 1997;38:868-873.
18. Ford JC, Hackney DB, Alsop DC, Jara H, Joseph PM, Hand CM, Black P. MRI characterization of diffusion coefficients in a rat spinal cord injury model. *Magn Reson Med* 1994;31:488-494.
19. Werring DJ, Clark CA, Parker GJM, Miller DH, Thompson AI, Barker GJ. A direct demonstration of both structure and function in the visual system: combining diffusion tensor imaging with functional magnetic resonance imaging. *Neuroimage* 1999;9:352-361.
20. Klingberg T, Hedehus Maj, Temple E, Salz T, Gabrieli JDE, Moseley ME, Poldrack RA. Microstructure of temporo-parietal white matter as a basis for reading ability: evidence from diffusion tensor magnetic resonance imaging. *Neuron* 2000;25:493-500.

21. Neil JJ, Shiran SI, Mc Kinstry RC, Schefft GL, Snyder AZ, Almli CR, Akbudak E, Aronovitz JA, Miller JP, Lee BCP, Conturo TE. Normal brain in human newborns: apparent diffusion coefficient and diffusion anisotropy measured by using diffusion tensor MR imaging. *Radiology* 1998;209:57-66.
22. Huppi PS, Maier SE, Peled S, Zientara GP, Barnes PD, Jolesz FA, Volpe JJ. Microstructural development of human newborn cerebral white matter assessed in vivo by diffusion tensor magnetic resonance imaging. *Pediatr Res* 1998;44:584-590.
23. Baratti C, Barnett AS, Pierpaoli C. Comparative MR imaging study of brain maturation in kittens with T1, T2, and the trace of the diffusion tensor. *Radiology* 1999;210:133-142.
24. Lythgoe MF, Busza AL, Calamante F, Sotak CH, King MD, Bingham AC, Williams SR, Gadian DG. Effects of diffusion anisotropy on lesion delineation in a rat model of cerebral ischemia. *Magn Reson Med* 1997;38:662-668.
25. de Crespigny AJ, Marks MP, Enzmann DR, Moseley ME. Navigated diffusion imaging of normal and ischemic human brain. *Magn Reson Med* 1995;33:720-728.
26. van Gelderen P, de Vleeschouwer MHM, DesPres D, Pekar J, van Zijl PCM, Moonen CTW. Water diffusion and acute stroke. *Magn Reson Med* 1994;31:154-163.
27. Warach S, Gaa J, Siewert B, Wielopolski P, Edelman RR. Acute human stroke studied by whole brain echo planar diffusion-weighted magnetic resonance imaging. *Ann Neurol* 1995;37:231-241.
28. Werring DJ, Clark CA, Barker GJ, Thompson AJ, Miller DH. Diffusion tensor imaging of lesions and normal-appearing white matter in multiple sclerosis. *Neurology* 1999;52:1626-1632.

29. Horsfield MA, Larsson HBW, Jones DK, Gass A. Diffusion magnetic resonance imaging in multiple sclerosis. *J Neurol, Neurosurg & Psych* 1998;64:S80-S84.
30. Bammer R, Augustin M, Strasser-Fuchs S, Seifert T, Kapeller P, Stollberger R, Ebner F, Hartung HP, Fazekas F. Magnetic resonance diffusion tensor imaging for characterizing diffuse and focal white matter abnormalities in multiple sclerosis. *Magn Reson Med* 2000;44:583-591.
31. Lim KO, Hedehus M, Moseley M, de Crespigny A, Sullivan EV, Pfefferbaum A. Compromised white matter tract integrity in schizophrenia inferred from diffusion tensor imaging. *Arch Gen Psychiatry*. 1999;56:367-374.
32. Werring DJ, Clark CA, Barker GJ, Miller DH, Parker GJM, Brammer MJ, Bullmore ET, Giampietro VP, Thompson AJ. The structural and functional mechanisms of motor recovery: complementary use of diffusion tensor and functional magnetic resonance imaging in a traumatic injury of the internal capsule. *J Neurol Neurosurg Psychiatry* 1998;65:863-869.
33. Jones DK, Dardis R, Ervine M, Horsfield MA, Jeffree M, Simmons A, Jarosz J, Strong AJ. Cluster analysis of diffusion tensor magnetic resonance images in human head injury. *Neurosurgery* 2000;47:306-313.
34. Le Bihan D. Diffusion NMR imaging. *Magn Reson Q* 1991;7:1-30.
35. Basser PJ. Inferring microstructural features and the physiological state of tissues from diffusion-weighted images. *NMR in Biomedicine* 1995;8:333-344.
36. Basser PJ, Pierpaoli C. Microstructural and physiological features of tissues elucidated by quantitative-diffusion-tensor MRI. *J Magn Reson B* 1996;111:209-219.

37. Pierpaoli C, Basser PJ. Toward a quantitative assessment of diffusion anisotropy. *Magn Reson Med* 1996;36:893-906.
38. Basser PJ, Pajevic S, Pierpaoli C, Duda J, Aldroubi A. In vivo fiber tractography using DT-MRI data. *Magn Reson Med* 2000;44:625-632.
39. Mori S, Crain BJ, Chacko VP, van Zijl PCM. Three-dimensional tracking of axonal projections in the brain by magnetic resonance imaging. *Ann Neurol* 1999;45:265-269.
40. Conturo TE, Lori NF, Cull TS, Akbudak E, Snyder AZ, Shimony JS, McKinstry RC, Burton H, Raichle ME. Tracking neuronal fiber pathways in the living human brain. *Proc Natl Acad Sci USA* 1999;96:10422-10427.
41. Poupon C, Clark CA, Frouin V, Regis J, Bloch I, Le Bihan D, Mangin JF. Regularization of diffusion-based direction maps for the tracking of brain white matter fascicles. *Neuroimage* 2000;12:184-195.
42. Xue R, van Zijl PCM, Crain BJ, Solaiyappan M, Mori S. In vivo three-dimensional reconstruction of rat brain axonal projections by diffusion tensor imaging. *Magn Reson Med* 1999;42:1123-1127.
43. Jones DK, Simmons A, Williams SCR, Horsfield MA. Non-invasive assessment of axonal fiber connectivity in the human brain via diffusion tensor MRI. *Magn Reson Med* 1999;42:37-41.
44. Papadakis NG, Xing D, Huang CLH, Hall LD, Carpenter TA. A comparative study of acquisition schemes for diffusion tensor imaging using MRI. *J Magn Reson* 1999;137:67-82.

45. Poonawalla AH, Karmonik C, Zhou XJ. Optimization of b-value and gradient orientation for diffusion tensor MRI. In "Proceedings: ISMRM Eighth Scientific Meeting, Denver, CO" 2000; p. 801.
46. Parker GJM, Werring DJ, Schnabel JA, Symms MR, Barker GJ. Noise reduction in diffusion tensor imaging - reducing systematic anisotropy errors. In "Proceedings: ISMRM Seventh Scientific Meeting, Philadelphia, PA" 1999; p. 1798.
47. Ordidge RJ, Helpert JA, Qing ZX, Knight RA, Nagesh A. Correction of motional artifacts in diffusion-weighted MR images using navigator echoes. *Magn Reson Imaging* 1994;12:455-460.
48. Alexander AL, Tsuruda JS, Parker DL. Elimination of eddy current artifacts in diffusion-weighted echo planar images: the use of bipolar gradients. *Magn Reson Med* 1997;38:1016-1021.
49. Reese TG, Weiskoff RM, Wedeen VJ. Diffusion NMR facilitated by a refocused eddy-current EPI pulse sequence. In "Proceedings: ISMRM Sixth Scientific Meeting, Sydney, Australia" 1998; p. 663.
50. Jezzard P, Barnett AS, Pierpaoli C. Characterization of and correction for eddy current artifacts in echo planar diffusion imaging. *Magn Reson Med* 1998;39:801-812.
51. Zhou XJ, Maier JK, Huff SJ, Mock BJ. Correction of image shift and distortion in diffusion-weighted echo planar imaging. In "Proceedings: ISMRM Seventh Scientific Meeting, Philadelphia, PA" 1999; p. 1818.
52. Haselgrove JC, Moore JR. Correction for distortion of echo-planar images used to calculate the apparent diffusion coefficient. *Magn Reson Med* 1996;36:960-964.

53. Symms MR, Barker GJ, Franconi F, Clark CA. Correction of eddy-current distortions in diffusion-weighted echo-planar images with a two-dimensional registration technique. In "Proceedings: ISMRM Fifth Scientific Meeting, Vancouver, Canada" 1997; p. 1723.
54. Stejskal EO, Tanner JE. Spin diffusion measurements: Spin echoes in the presence of a time-dependent field gradient. J Chem Physics 1964;42:288-292.
55. Press WH, Flannery BP, Teukolsky SA, Vetterling WT. Numerical recipes in C: The art of scientific computing. Second edition. Cambridge: Cambridge University Press, 1992.
56. Westin CF, Peled S, Gubjartsson H, Kikinis R, Jolesz FA. Geometrical diffusion measures for MRI from tensor basis analysis. In "Proceedings: ISMRM Fifth Scientific Meeting, Vancouver, Canada" 1997; p. 1742.
57. Alexander AL, Hasan K, Kindlmann G, Parker DL, Tsuruda JS. A geometric analysis of diffusion tensor measurements of the human brain. Magn Reson Med 2000;44:283-291.
58. Pajevic C, Pierpaoli C. Color schemes to represent the orientation of anisotropic tissues from diffusion tensor data: application to white matter fiber tract mapping in the human brain. Magn Reson Med 1999;42:526-540.
59. Mattiello J, Basser PJ, LeBihan D. Analytical expressions for the b matrix in NMR diffusion imaging and spectroscopy. J Magn Reson 1993;108:131-141.